Scripta Materialia 272 (2026) 117073

Contents lists available at ScienceDirect

Scripta Materialia

journal homepage: www.journals.elsevier.com/scripta-materialia

Solid solutions limited by grain-boundary solute clustering in ultrafine-grained alloys

Pavel Nikitin [a,*], Maxime Guinel de France [b], Frederic Sansoz [a,*]

[a] Department of Mechanical Engineering, The University of Vermont, Burlington, VT 05405, USA
[b] Electron Microscope Facility, Dartmouth College, Hanover, NH 03755, USA

ARTICLE INFO

Keywords:
Ultrafine-grained alloys
Solute clustering
Grain boundaries
Magnetron sputtering
Density-functional theory
Molecular dynamics

ABSTRACT

Immiscible Ag-Cu alloys exhibit complex behavior due to varying Cu solid solubilities reported under equilibrium and metastable conditions. In ultrafine-grained alloys, these limits are further complicated by a high fraction of grain boundaries, where solute atoms tend to segregate and, in some cases, form clusters. This study investigates the influence of Cu solute segregation and clustering on solid-solution limits in ultrafine-grained Ag-Cu alloys synthesized by magnetron sputtering with varying Cu content. X-ray diffraction peak shifts reveal a solid-solution concentration plateau for Cu contents from 4.9 to 11.7 at %, in contrast to the peak shifts predicted by density-functional theory for Ag-Cu alloys. Scanning transmission electron microscopy further reveals limited solid solubility and the formation of numerous Cu-rich clusters at grain boundaries. Atomistic simulations demonstrate that such limited solubility does not arise from grain boundary segregation alone, but only when strong solute-solute interactions promote the formation of grain-boundary Cu solute clusters.

There are several physical factors that contribute to the complexity of the binary Ag-Cu system. Under equilibrium conditions at the eutectic temperature of 779.1 °C, the maximum solubility of Cu in Ag is 8.27 at.% [1], while at room temperature, the mutual solubility of Ag and Cu is <1 at.% [2,3]. This pronounced immiscibility, however, is unexpected, as both elements have similar electronegativities, share the same face-centered cubic (FCC) crystal structure, and exhibit an atomic size mismatch of approximately 13 %, which satisfy the Hume-Rothery criterion for solid solution formation [4]. Nevertheless, various non-equilibrium processing techniques, such as vapor deposition, mechanical alloying, and ion beam mixing, have been extensively employed to synthesize metastable Ag-Cu alloys with extended solid solubility [2,3,5–9]. For instance, F. Misják et al. have produced Cu-Ag alloys by thermal evaporation with mutual solubility of Ag and Cu of 10 at.% [3]. S. Gohil et al. have reported the sputtering of Ag-Cu thin films at room temperature, achieving a Cu solubility of up to 13 at.% with an additional formation of a hexagonal (4H) phase [2]. Dirks et al. have reported Cu solubility of 10 at.% in vapor-deposited thin films [10]. Ma *et al.* have observed a formation of amorphous Ag-Cu solid solutions [5,6].

All these phenomena have been demonstrated for alloys with a high Cu content, often close to the eutectic composition of Ag-40Cu, within the spinodal decomposition region of the Ag-Cu phase diagram, where thermodynamic effects dominate and lead to the decomposition of the solid solutions and the formation of Ag- and Cu-rich phases [11–13]. Meanwhile, recent molecular dynamics (MD) simulations have shown that at lower Cu concentrations (up to 15 at.%), Cu segregates to grain boundaries (GBs), with the dilute limit depending on the Ag grain size [14], and exhibits complex solute-solute interaction behavior [15,16]. In ultrafine-grained and nanocrystalline materials, the GB fraction becomes comparable to the grain interior fraction and must be accounted for in the analysis. The intrinsic GB structure of Ag-Cu polycrystals also varies strongly with composition, evolving from random distributions of GB solutes in Ag-rich alloys [17,18] to ordered GB complexions and even amorphous interface films with Cu-rich alloys [19,20]. Given that Cu segregates to Ag GBs and exhibits complex solute-solute interactions, these effects are expected to significantly influence the solid solution limits of Ag-Cu alloys as well [21]. There are, however, no experimental studies addressing these effects.

In this study, Ag-Cu alloys with Cu contents up to 12 at.% were synthesized via magnetron co-sputtering. Microstructural characterization by X-ray diffraction (XRD) and scanning transmission electron microscopy (STEM) reveal an intragranular solid-solution concentration plateau for Cu contents extending from 4.9 to 11.7 at.%. MD simulations

---

* Corresponding authors.
E-mail addresses: pavel.nikitin@uvm.edu (P. Nikitin), frederic.sansoz@uvm.edu (F. Sansoz).

https://doi.org/10.1016/j.scriptamat.2025.117073
Received 18 July 2025; Received in revised form 23 September 2025; Accepted 23 October 2025

further demonstrate that the observed maximum solubility limit of Cu in ultrafine-grained Ag arises from attraction interactions between Cu solute atoms segregated to the GBs, which promote clustering and ultimately limit further dissolution into the Ag matrix.

Ag-Cu alloys were prepared by direct-current (DC) magnetron co-sputtering of Ag (99.99 % purity) and Cu (99.999 % purity) targets. B-doped Si (100) wafers were used as substrates for deposition. The base pressure was approximately 5×10^{-4} Pa, and the Ar pressure (99.999 % purity) during deposition was maintained at 1.6 Pa. The distance between the targets and the substrate was set at 8 cm. To control the Cu content in the sputtered Ag-Cu alloys, two power units were used: the power applied to the Ag target was fixed at 200 W, while the power applied to the Cu target was varied up to 50 W. To promote uniform distribution of Cu, the substrate was rotated at 15 rpm during deposition. The deposition time was 40 min, producing foils approximately 5 μm thick with a strongly textured (111) microstructure, as detailed in our recent work [22]. No substrate cooling was enforced during the deposition. Using the methodology described in [22], the deposition temperature was estimated to be in the range of 60–100 °C. The Cu content in the sputtered alloys, measured by energy-dispersive X-ray spectroscopy (EDS, Oxford Instruments) in a field-emission scanning electron microscope (FESEM, Zeiss VP300), was found to be 2.0, 4.9, 8.0, and 11.7 at.%. Furthermore, a ThermoFisher Scientific Helios 5CX Dual-Beam (SEM-focus-ion beam) microscope was used to fabricate 50–70 nm thick planar specimens for STEM. STEM analysis was performed using a ThermoFisher Scientific Talos F200i STEM, equipped with a Dual-X EDS (EDX) system.

XRD analysis was performed using a Rigaku Miniflex II diffractometer with Cu-K radiation, the step size of 0.02°, and the scanning speed of 1°/min. Also, the experimental XRD patterns were compared to simulated ones based on density-functional-theory (DFT) calculations. To do this, pure Ag and Cu, and Ag-Cu alloys supercells ($3 \times 3 \times 3$) with different Cu concentrations were fully relaxed (ionic + cell relaxation) using DFT, and the XRD patterns of these structures were obtained using the software VESTA (Powder Diffraction Pattern) [23–25]. DFT simulations were performed with the software VASP [26]. Projector augmented wave (PAW) pseudopotentials were used [27]. The electron exchange-correlation was described using the GGA-PBE functional [28]. The plane-wave cutoff energy of 600 eV, Brillouin zone sampling with a k-point grid of $2\pi \times 0.02$ Å^{-1} resolution and convergence criteria of 1×10^{-5} eV per atom for total energies and 1×10^{-2} eV Å^{-1} for forces were employed.

The representative XRD pattern of the Ag-Cu alloy (2 at.% Cu) is shown in Fig. 1a. It exhibits a main (111) peak along with (200), (220), (311), and (222) secondary peaks. All the peaks match those of the reference FCC Ag. The full diffraction patterns of the Ag-4.9 at.% Cu and Ag-11.7 at.% Cu alloys are not shown here, as they do not qualitatively differ from that of Ag-2 at. % Cu (Fig. 1a). However, a zoomed-in view of the (111) peak is presented for all the alloys (Fig. 1b) with a reference value of pure Ag (dashed vertical line). The main (111) peak shifts to 38.22° for the Ag-2 at.% Cu and further to 38.28° for both Ag-4.9 at.% Cu and Ag-11.7 at.% Cu, reaching its limit. In this case, the rightward shift of the peaks can be attributed to Cu atoms substituting Ag atoms in the lattice, indicating the formation of a solid solution. It should be noted, however, that peak shifts can also result from residual stresses induced during magnetron sputtering [29–32]. According to Ref. [29], the calculation of residual stresses in strongly textured films requires advanced techniques beyond standard XRD analysis and is not the focus of this study. Therefore, in our further analysis, to minimize the influence of stress-related effects, the peak of pure Ag deposited under the same sputtering conditions as the Ag-Cu alloys (Fig. 1b, green line) was used as the reference.

Fig. 2 shows the trend of the (111) peak shifts in the experimental Ag-Cu alloys with those predicted by DFT. The (111) peak shift of the Ag-8 at.% Cu alloy was included for additional comparison. The discrepancy in the (111) peak shifts becomes noticeable already at 2 at. % Cu and becomes more pronounced with increasing Cu concentration.

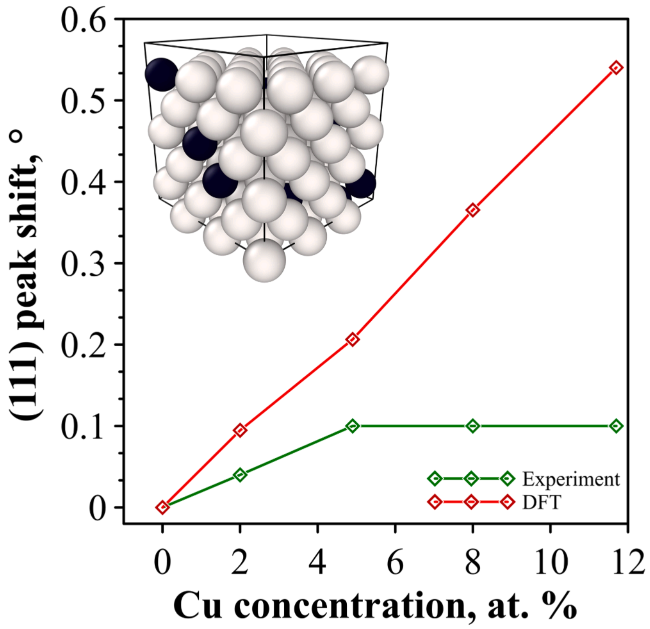

Fig. 2. Experimental (111) XRD peak positions in the sputtered Ag-Cu alloys compared to density-functional-theory (DFT) predictions on an FCC solution supercell shown in inset, where Ag and Cu atoms are colored in light grey and black, respectively.

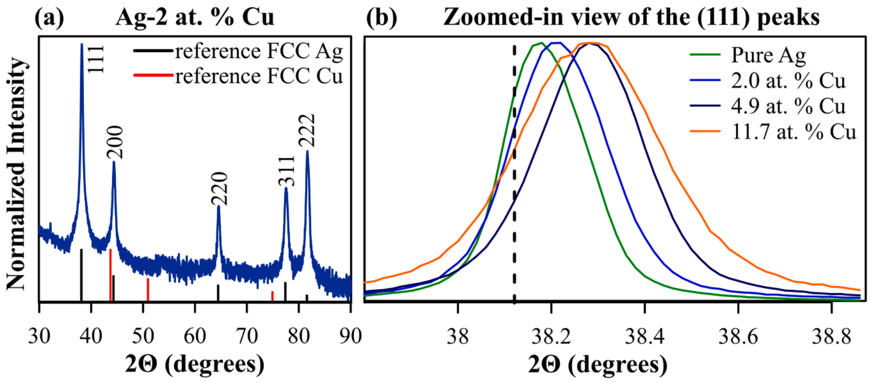

Fig. 1. XRD analysis of the sputtered Ag-Cu alloys. (a) XRD pattern of the Ag-2 at.% Cu alloy (logarithmic scale is used for better visualization of secondary peaks); (b) Zoomed-in view of the (111) peak for the Ag-Cu alloys.

At 4.9 at.% Cu, the experimental results significantly deviate from the DFT-predicted trend, forming a plateau in the concentration range of 4.9 to 11.7 at.% Cu (Fig. 2).

Additionally, we used the XRD data to estimate the fraction of Cu dissolved into the Ag matrix using Vegard's law [33] such as:

$$X_{Cu} = \left(a_{alloy} - a_{Ag}\right) / \left(a_{Cu} - a_{Ag}\right) \tag{1}$$

where the a parameters are the respective lattice constants determined from the experimental XRD (111) peak positions and Bragg's law. The results of Eq. (1) are presented in Table 1 for all films synthesized in this study. For the Ag-2 % Cu alloy, Eq. (1) predicts that 0.9 % Cu is in solid solution with the Ag matrix, and this value increases with higher Cu content. However, for alloys with Cu contents between 4.9 % and 11.7 %, Table 1 shows that the fraction of Cu dissolved in the Ag matrix reaches a plateau at 2.2 %.

It is important to note that the excess free volume at GBs was not considered in Eq (1). As a result, the above analysis does not account for the influence Cu atoms segregated to GBs. This point is important because atomistic simulations have shown that GB excess free volume decreases linearly with the local Cu concentration in Ag polycrystals [14]. To study the possible segregation of Cu atoms to GBs, we conducted STEM-EDX on specimens containing 2 %, 4.9 %, and 11.7 % Cu. To evaluate the Cu solid solution in each specimen, we analyzed the elemental composition of five individual Ag grains per specimen (examples of analyzed regions are marked with a yellow square in Fig. 3a and 3c). The STEM results shown in Table 1 indicate that the average Cu content inside grains is close to the Cu solid solution estimated by XRD using Eq. (1). Furthermore, STEM-EDX images of the Ag-2 at. % Cu and Ag-11.7 at. % Cu alloys in Fig. 3 reveal ultrafine Ag grains with diameters approximately ranging from 100 nm to 200 nm. Notably, the sputtered materials contain Cu-rich clusters and nanoprecipitates [34–36], which are typical of coarse-grained Ag-Cu alloys. These features form either near GB junctions, as shown in the inset of Fig. 3a, or along individual GBs, where they appear as necklace-like clusters in Fig. 3b A detailed STEM-EDX analysis of these clusters and nanoprecipitates, including line profile measurements, was reported in our previous study [37]. Also, Fig. 3 and Table 1 show that Cu clusters formed at all concentrations, which suggests that the solubility limits were exceeded, even at low Cu contents.

The presence of both Cu-rich clusters and nanoprecipitates and solid solution grains at all concentrations is significant for several reasons. First, it confirms that these alloys exhibit limited solubility. Second, the observed solid solution limits are directly linked to the formation of Cu clusters and nanoprecipitates along the GB network. Third, the formation of Cu clusters was not anticipated in previous MC/MD simulation studies of annealed Ag-Cu polycrystals [14,17,18,38]. Notably, these simulations predicted only weak Cu-Cu interactions at GBs [14], which may explain the absence of clustering in those models. In our recent work [22], however, we demonstrated a previously unrecognized pathway for GB solute clustering, driven not by individual solute-solute interactions but by collective solute-cluster interactions. In this mechanism, once a solute cluster is formed, it could act as a preferential site that strongly attracts additional solute atoms.

In the present study, we show atomistic simulations that demonstrate pronounced Cu clustering at the interface of a high-energy Σ9(221) symmetric tilt bicrystal in Ag, which contrasts with the Cu segregation behavior predicted in previous atomistic simulations [15]. To achieve this, we employed the optimized EAM-X (embedded atom method) potential developed by Daw and Chandross [39,40] to model the Ag-Cu interactions. This potential introduces a cross-interaction parameter χ (0.106 for Ag-Cu) and enables the simulation of GB segregation alone when the parameter has a negative sign, and solute clustering when it is positive. The parameter χ is fitted to binary dilute heats of solution, and the sign of χ controls the balance between clustering and ordering tendencies. Readers interested in the detailed formulation and justification of this parameter are referred to the original paper [40]. Hybrid Monte Carlo/molecular dynamics (MC/MD) simulations implemented in the Large-scale Atomic/Molecular Massively Parallel Simulator (LAMMPS) code [41] were performed at a temperature of 500 K using the same parameters described elsewhere [16].

To explore the effects of both segregation and clustering of Cu solutes on the limits of solid solubility, we examined two representative cases: a low Cu concentration of 2 at.% and a high concentration of 11.7 at.%. As can be seen from Fig. 4a and b, a negative value of the cross-interaction parameter χ of –0.106 results in homogeneous GB segregation, as evidenced by the significantly higher Cu concentration at the GBs compared to the Ag grains, corresponding to 10 at.% for the Ag-2 at.% Cu bicrystal and 22.7 at.% for the Ag-11.7 at.% Cu bicrystal. However, GB segregation alone does not impose a limit on solid solubility, as the Cu content within the Ag grains increases proportionally with the overall Cu concentration (Fig. 4e). This indicates that segregation, in the absence of clustering, is insufficient to establish a solubility plateau.

When the cross-interaction parameter χ is set to a positive value of +0.106, Cu solutes exhibit a clear tendency to form clusters, and GB solute clusters become well-defined. At 2 at.% Cu, the GB clusters are only a few bonded Cu atoms, as highlighted by red arrows in Fig. 4c, and become significantly larger in size at high solute concentration as shown in Fig. 4d. This observation is consistent with our recent work [22], which showed that solute-cluster attraction is weak for small clusters (up to 6 atoms) but increases markedly as the cluster size grows. At 2 at. % Cu, the number of solutes segregated to GBs is insufficient to form clusters of critical size. At higher concentrations, however, enough solutes are available to form stable clusters that act as strong segregation sites, attracting additional Cu atoms in a snowball-like manner. This process limits the solute content in the surrounding solid solution within the Ag grains, as observed in Fig. 4d. At the same time, as demonstrated in [37] using the same MC/MD approach, these Cu solute clusters at GBs are amorphous, with adjacent FCC Cu inclusions acting as precursors for the growth of ordered Cu nanoprecipitates.

To quantify the influence of GB clustering on solid solubility, the solid solution Cu content was evaluated for concentrations between 2 and 11.7 at.%, as shown in Fig. 4e. These results reveal an intragranular solid-solution concentration plateau at approximately 1.5 ± 0.5 at.% within the Cu concentration range of 4.9 to 15 at.% Cu. The estimated error of ±0.5 at.% accounts for the diffuse nature of large clusters, whose boundaries may extend slightly beyond the GB region, depending on how their edges are included in the analysis. The obtained simulation results are in close agreement with the experimental data, although not in exact quantitative correspondence. This discrepancy may be attributed to the use of a high-energy Σ9 (221) GB in the simulations, whereas the experimental specimens contain a distribution of GBs with varying energies.

In conclusion, these findings underscore the critical role of solute clustering at GBs in establishing the limits of solid solubility in ultrafine-grained alloys and provide new insight into the thermodynamic and kinetic factors governing alloy stability at the nanoscale. While GB segregation alone does not limit solubility, the formation of Cu-rich clusters, driven by strong solute-solute and solute-cluster interactions [22], was found to be essential for the emergence of a solubility plateau.

Table 1
Summary of experimental results in the sputtered Ag-Cu alloys by XRD using Eq. (1) and STEM-EDX analysis inside individual grains away from GBs.

Total Cu content (at. %)	Cu solute (at.%) by Eq. (1)	Intragranular Cu solute (at.%) by STEM
2.0	0.9	1.0 ± 0.1
4.9	2.2	2.7 ± 0.3
8.0	2.2	–
11.7	2.2	2.8 ± 0.3

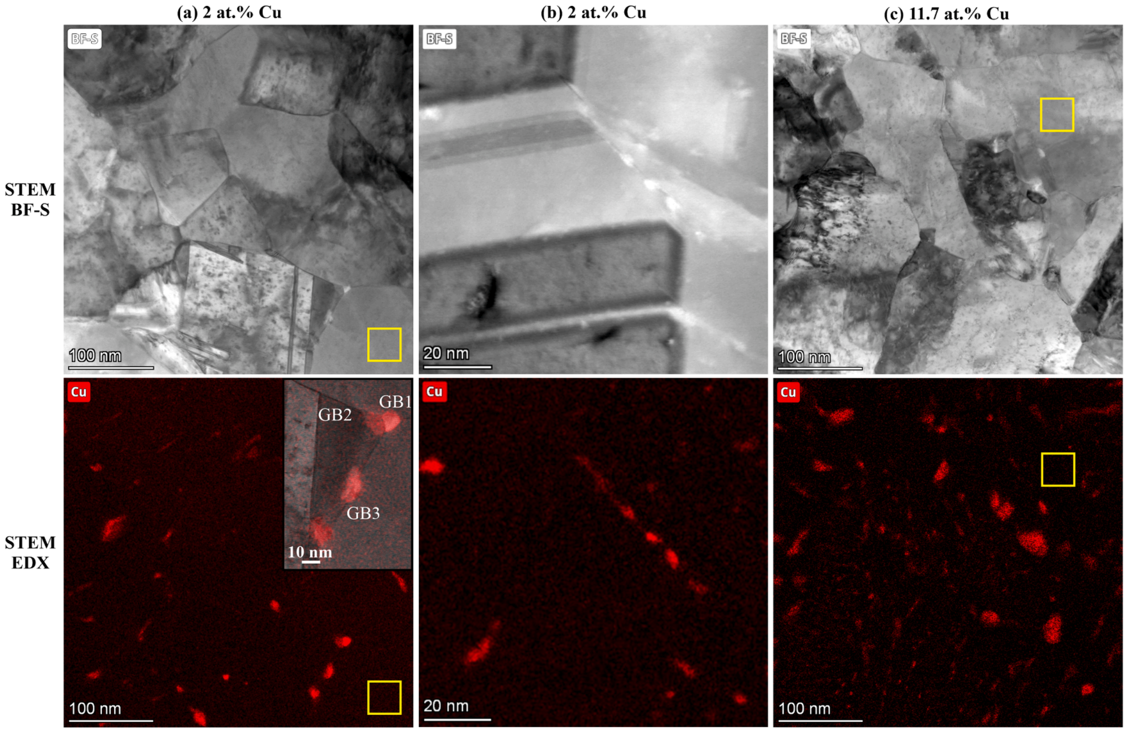

Fig. 3. Pairs of brightfield (BF-S) STEM images and EDX elemental maps recorded from the sputtered (a-b) Ag-2 at.% Cu alloy and (c) Ag-11.7 at.% Cu alloy. Yellow squares indicate locations within Ag grains where EDX analysis was performed to measure Cu concentration. The inset image in (a) is a mixed BF-S and EDX close-up image focused on three GB solute clusters seen in the lower-right region.

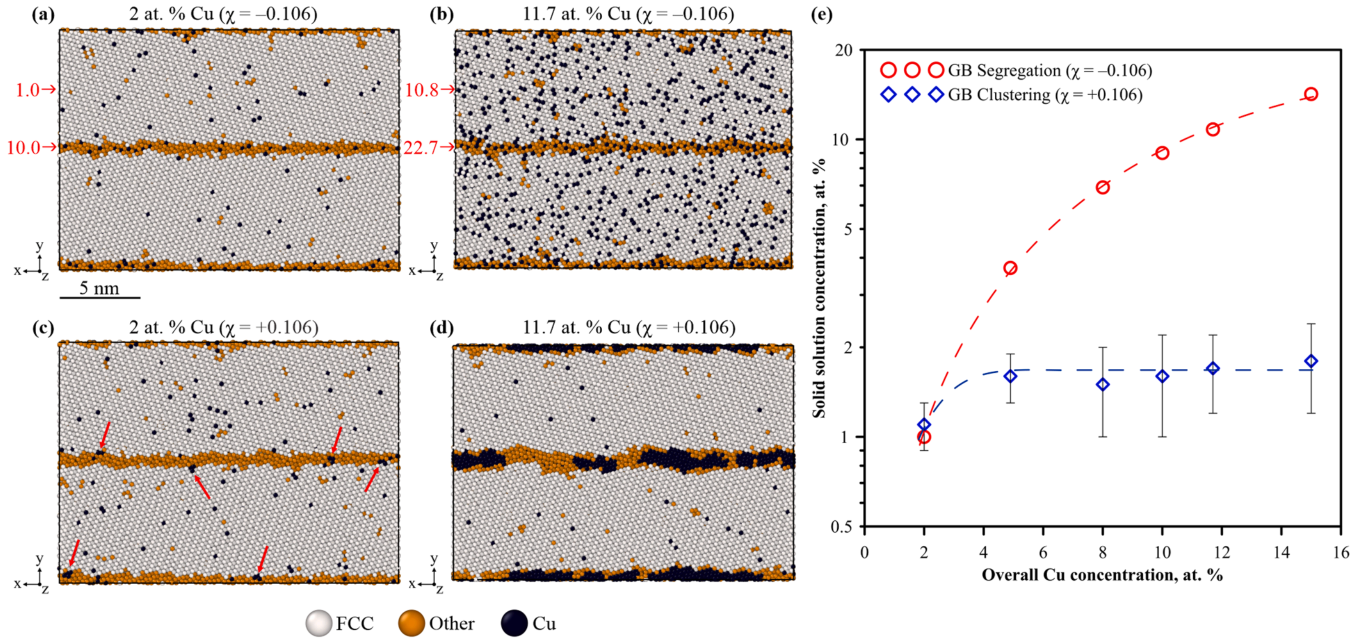

Fig. 4. Hybrid EAM-X MC/MD simulations of the effects of GB solute segregation (a, b) and GB solute clustering (c, d) on Cu solid solution concentration in high-energy Σ9 (221) GBs at overall Cu concentrations of 2 and 11.7 at.%. The local solute compositions (at.%) in the grain interior and the two GBs are indicated in red color. (e) Solid solution concentration as a function of overall Cu concentration for either GB segregation or GB clustering simulations (dashed lines are included for visual guidance only).

CRediT authorship contribution statement

Pavel Nikitin: Writing – review & editing, Writing – original draft, Methodology, Investigation, Formal analysis, Data curation, Conceptualization. **Maxime Guinel de France:** Visualization, Investigation, Data curation. **Frederic Sansoz:** Writing – review & editing, Writing – original draft, Supervision, Project administration, Funding acquisition, Formal analysis, Conceptualization.

Declaration of competing interest

The authors declare that they have no known competing financial interests or personal relationships that could have appeared to influence the work reported in this paper.

Acknowledgements

PN and FS acknowledge support by the U.S. Department of Energy (DOE) under grant no DE-SC0020054. The Zeiss VP300 and the ThermoFisher Scientific Talos F200i instruments used in this study were acquired through the National Science Foundation (NSF) under MRI grants no 1828371 to the University of Vermont and no 2213198 to Dartmouth College, respectively. All simulations have been performed on the supercomputer Perlmutter at the National Energy Research Scientific Computing Center (NERSC), a U.S. Department of Energy Office of Science User Facility located at Lawrence Berkeley National Laboratory, operated under Contract No DE-AC02-05CH11231.

References

[1] F.H. Hayes, H.L. Lukas, G. Effenberg, G. Petzow, A thermodynamic optimisation of the Cu-Ag-Pb system, Int. J. Mater. Res. 77 (11) (1986) 749–754, https://doi.org/10.1515/ijmr-1986-771108.
[2] S. Gohil, R. Banerjee, S. Bose, P. Ayyub, Influence of synthesis conditions on the nanostructure of immiscible copper–silver alloy thin films, Scr. Mater. 58 (10) (2008) 842–845, https://doi.org/10.1016/j.scriptamat.2007.12.043.
[3] F. Misják, P.B. Barna, G. Radnóczi, Growth of nanocomposite in eutectic Cu–Ag films, Thin Solid Films 518 (15) (2010) 4247–4251, https://doi.org/10.1016/j.tsf.2009.12.095.
[4] W. W. Hume-Rothery, G. Mabbott, K.M. Channel Evans, H.C.H. Carpenter, The freezing points, melting points, and solid solubility limits of the alloys of sliver and copper with the elements of the b sub-groups Philos. Trans. R. Soc. Lond. A 233 (721–730) (1934) 1–97, https://doi.org/10.1098/rsta.1934.0014. Containing Papers of a Mathematical or Physical Character
[5] H.W. Sheng, G. Wilde, E. Ma, The competing crystalline and amorphous solid solutions in the Ag–Cu system, Acta Mater. 50 (3) (2002) 475–488, https://doi.org/10.1016/S1359-6454(01)00374-3.
[6] E. Ma, Alloys created between immiscible elements, Prog. Mater. Sci. 50 (4) (2005) 413–509, https://doi.org/10.1016/j.pmatsci.2004.07.001.
[7] B.Y. Tsaur, S.S. Lau, J.W. Mayer, Continuous series of metastable Ag-Cu solid solutions formed by ion-beam mixing, Appl. Phys. Lett. 36 (10) (1980) 823–826, https://doi.org/10.1063/1.91331.
[8] K. Uenishi, K.F. Kobayashi, K.N. Ishihara, P.H. Shingu, Formation of a super-saturated solid solution in the AgCu system by mechanical alloying, Mater. Sci. Eng.: A 134 (1991) 1342–1345, https://doi.org/10.1016/0921-5093(91)90987-X.
[9] R. Najafabadi, D.J. Srolovitz, E. Ma, M. Atzmon, Thermodynamic properties of metastable Ag-Cu alloys, J. Appl. Phys. 74 (5) (1993) 3144–3149, https://doi.org/10.1063/1.354582.
[10] A.G. Dirks, J.J. van den Broek, P.E. Wierenga, Mechanical properties of thin alloy films: ultramicrohardness and internal stress, J. Appl. Phys. 55 (12) (1984) 4248–4256, https://doi.org/10.1063/1.333027.
[11] O.P. Pandey, S.N. Ojha, S. Lele, On spinodal boundaries of the AgCu system, Scr. Metall. Mater. 29 (8) (1993) 1131–1134, https://doi.org/10.1016/0956-716X(93)90190-4.
[12] G. Ummethala, P. Bandaru, S. Chatterjee, S. Dutta-Gupta, S.R.K. Malladi, A study of the spinodal decomposition of AgCu alloy films using in situ transmission electron microscopy, Mater. Charact. 216 (2024) 114297, https://doi.org/10.1016/j.matchar.2024.114297.
[13] G. Radnóczi, E. Bokányi, Z. Erdélyi, F. Misják, Size dependent spinodal decomposition in Cu-Ag nanoparticles, Acta Mater. 123 (2017) 82–89, https://doi.org/10.1016/j.actamat.2016.10.036.
[14] F. Sansoz, X. Ke, Hall–petch strengthening limit through partially active segregation in nanocrystalline Ag-Cu alloys, Acta Mater. 225 (2022) 117560, https://doi.org/10.1016/j.actamat.2021.117560.
[15] T. Nenninger, F. Sansoz, Local atomic environment analysis of short and long-range solute-solute interactions in a symmetric tilt grain boundary, Scr. Mater. 222 (2023) 115045, https://doi.org/10.1016/j.scriptamat.2022.115045.
[16] T. Nenninger, F. Sansoz, Solute clustering in polycrystals: unveiling the interplay of grain boundary junction and long-range solute attraction effects, Acta Mater. 290 (2025) 120946, https://doi.org/10.1016/j.actamat.2025.120946.
[17] Z. Pan, F. Sansoz, Heterogeneous solute segregation suppresses strain localization in nanocrystalline Ag-Ni alloys, Acta Mater. 200 (2020) 91–100, https://doi.org/10.1016/j.actamat.2020.08.074.
[18] Z. Pan, V. Borovikov, M.I. Mendelev, F. Sansoz, Development of a semi-empirical potential for simulation of Ni solute segregation into grain boundaries in Ag, modelling and simulation, Mater. Sci. Eng. 26 (7) (2018) 075004, https://doi.org/10.1088/1361-651X/aadea3.
[19] N.J. Peter, M.J. Duarte, C. Kirchlechner, C.H. Liebscher, G. Dehm, Faceting diagram for Ag segregation induced nanofaceting at an asymmetric Cu tilt grain boundary, Acta Mater. 214 (2021) 116960, https://doi.org/10.1016/j.actamat.2021.116960.
[20] A. Li, I. Szlufarska, Morphology and mechanical properties of nanocrystalline Cu/Ag alloy, J. Mater. Sci. 52 (8) (2017) 4555–4567, https://doi.org/10.1007/s10853-016-0700-3.
[21] E. Hondros, M. Seah, The theory of grain boundary segregation in terms of surface adsorption analogues, Metall. Trans. A 8 (9) (1977) 1363–1371.
[22] P. Nikitin, F. Sansoz, Size-dependent attraction of Cu solutes to clusters formed at Ag grain boundaries, Phys. Rev. Mater. 9 (9) (2025) 093603, https://doi.org/10.1103/t7qb-g8n6.
[23] P. Nikitin, I. Zhukov, D. Tkachev, Y. Abzaev, E. Marchenko, A. Vorozhtsov, Experimental and theoretical study of ultra-hard AlMgB14-TiB2 composites: structure, hardness and self-lubricity, Materials 15 (23) (2022) 8450.
[24] N.S. Evseev, A.E. Matveev, P.Y. Nikitin, Y.A. Abzaev, I.A. Zhukov, A theoretical and experimental investigation on the SHS synthesis of (HfTiCN)-TiB2 high-entropy composite, Ceram. Int. 48 (11) (2022) 16010–16014, https://doi.org/10.1016/j.ceramint.2022.02.144.
[25] K. Momma, F. Izumi, VESTA 3 for three-dimensional visualization of crystal, volumetric and morphology data, J. Appl. Crystallogr. 44 (6) (2011) 1272–1276, https://doi.org/10.1107/S0021889811038970.
[26] G. Kresse, J. Furthmüller, Efficiency of ab-initio total energy calculations for metals and semiconductors using a plane-wave basis set, Comput. Mater. Sci. 6 (1) (1996) 15–50, https://doi.org/10.1016/0927-0256(96)00008-0.
[27] P.E. Blöchl, Projector augmented-wave method, Phys. Rev. B 50 (24) (1994) 17953–17979, https://doi.org/10.1103/PhysRevB.50.17953.
[28] J.P. Perdew, K. Burke, M. Ernzerhof, Generalized gradient approximation made simple, Phys. Rev. Lett. 77 (18) (1996) 3865–3868, https://doi.org/10.1103/PhysRevLett.77.3865.
[29] J. Yeom, G. Lorenzin, C. Cancellieri, J. Janczak-Rusch, Evaluation of residual stresses in Cu/Mo, Cu/Nb nanomultilayers with a strong fiber texture, Mater. Lett. 352 (2023) 135074, https://doi.org/10.1016/j.matlet.2023.135074.
[30] G. Lorenzin, L.P.H. Jeurgens, C. Cancellieri, Stress tuning in sputter-grown Cu and W films for Cu/W nanomultilayer design, J. Appl. Phys. 131 (22) (2022), https://doi.org/10.1063/5.0088203.
[31] G. Lorenzin, F.F. Klimashin, J. Yeom, Y. Hu, J. Michler, J. Janczak-Rusch, V. Turlo, C. Cancellieri, Effect of residual stress and microstructure on mechanical properties of sputter-grown Cu/W nanomultilayers, APL Mater. 12 (10) (2024), https://doi.org/10.1063/5.0226849.
[32] N. Maréchal, E.a. Quesnel, Y. Pauleau, Silver thin films deposited by magnetron sputtering, Thin Solid Films 241 (1–2) (1994) 34–38.
[33] L. Vegard, Die konstitution der Mischkristalle und die raumfüllung der Atome, Z. Phys. 5 (1) (1921) 17–26, https://doi.org/10.1007/BF01349680.
[34] R.G. Rose, The precipitation of copper from a silver-5.5% copper solid solution at 220 °C*, Acta Metall. 5 (7) (1957) 404–405, https://doi.org/10.1016/0001-6160(57)90010-X.
[35] D. Hamana, L. Boumaza, Precipitation mechanism in Ag–8wt.% Cu alloy, J. Alloys Compd. 477 (1) (2009) 217–223, https://doi.org/10.1016/j.jallcom.2008.10.063.
[36] S. Colombo, P. Battaini, G. Airoldi, Precipitation kinetics in Ag–7.5wt.% Cu alloy studied by isothermal DSC and electrical-resistance measurements, J. Alloys Compd. 437 (1) (2007) 107–112, https://doi.org/10.1016/j.jallcom.2006.07.076.
[37] P. Nikitin, M. Guinel de France, F. Sansoz, The physical origin of heterogeneous solute clustering and nanoprecipitation at grain boundaries in ultrafine-grained immiscible alloys, Scr. Mater. 270 (2026) 116939, https://doi.org/10.1016/j.scriptamat.2025.116939.
[38] X. Ke, J. Ye, Z. Pan, J. Geng, M.F. Besser, D. Qu, A. Caro, J. Marian, R.T. Ott, Y. M. Wang, F. Sansoz, Ideal maximum strengths and defect-induced softening in nanocrystalline-nanotwinned metals, Nat. Mater. 18 (11) (2019) 1207–1214, https://doi.org/10.1038/s41563-019-0484-3.
[39] M.S. Daw, M. Chandross, Simple parameterization of embedded atom method potentials for FCC metals, Acta Mater. 248 (2023) 118771, https://doi.org/10.1016/j.actamat.2023.118771.
[40] M.S. Daw, M. Chandross, Simple parameterization of embedded atom method potentials for FCC alloys, Acta Mater. 248 (2023) 118772, https://doi.org/10.1016/j.actamat.2023.118772.
[41] S. Plimpton, Fast parallel algorithms for short-range molecular dynamics, J. Comput. Phys. 117 (1) (1995) 1–19, https://doi.org/10.1006/jcph.1995.1039.